Shore-based photogrammetry of river ice

Daniel Bourgault

Abstract: A simple and inexpensive method using a shore-based commercially available digital camera is developed to monitor river ice. The method was tested in a section of the St. Lawrence River, near Québec City, where tidal currents induce large changes in the ice distribution. It is shown that high resolution objective and quantitative information, such as the ice extent, spatiotemporal variability, and current fields, can be determined from the georectified images. The method proposed may provide an alternative to costly aerial surveys and other more sophisticated remote sensing techniques.

Key words: photogrammetry, georectification, river ice, monitoring.

Résumé : Une méthode simple et peu coûteuse est développée qui utilise un appareil photographique facilement disponible sur le marché installé sur la berge pour surveiller la glace de rivière. Cette méthode a été testée sur une section du fleuve Saint-Laurent, près de la Ville de Québec, où les courants de marée induisent d'importants changements dans la distribution des glaces. Il est montré que des données objectives et quantitatives à haute résolution, telle que l'étendue des glaces, la variabilité spatiotemporelle et les champs de courants peuvent être déterminés à partir d'images géocorrigées. La méthode proposée peut fournir une alternative aux relevés aériens dispendieux et aux autres techniques de télédétection plus sophistiquées.

Mots-clés : photogrammétrie, géorectification, glace de rivière, surveillance.

[Traduit par la Rédaction]

Introduction

Monitoring river ice is important for navigation and for predicting and preventing ice jams and floods. Monitoring techniques include shore-, ship-, and aerial-based visual surveys; in situ measurements; radar remote sensing; and acoustic measurements (Weber et al. 2003; Morse et al. 2003; Environment Canada 2005). In Canada, visual surveys, based on standardized procedures (Environment Canada 2005), are largely used to produce river ice reports. However, this method is somewhat subjective and qualitative as it relies on the observer's expertise. Furthermore, visual surveys cannot be automated as they require the observer as well as crew members to operate the observing platform (i.e., airplane, helicopter, ship). Other methods that rely on instrumentation are objective, quantitative, and can be automated, but also have their limitations. For example, moored upward-looking acoustic Doppler current profilers can provide accurate and reliable continuous measurements of the ice thickness and velocity at one location (Morse et al. 2003), but cannot provide the spatial coverage. On the other hand, remote sensing observations can provide a large spatial coverage of the ice (Weber et al. 2003), but cannot be easily used to measure ice thickness and velocity. As noted by Morse et al. (2003), a combination of in situ, acoustic, and remote sensing techniques could provide a more complete, objective, and quantitative picture of river ice distribution and dynamics. However, existing remote sensing tools, such as RADARSAT (MacDonald, Dettwiler and Associates Ltd., Vancouver, B.C.), can be both expensive and challenging to implement in a monitoring program.

This study was motivated by the need for a simple, inexpensive, and objective remote sensing method for monitoring river ice. The method proposed is based on shore-based still camera imagery. The use of commercially available shore-based cameras to obtain quantitative visualization of sea surface patterns, such as those induced by waves breaking on beaches, fronts or internal waves, has already been developed and tested by Holland et al. (1997) and Pawlowicz (2003) and applied by Bourgault and Kelley (2003). The method employed here is essentially the same as in these studies, except that it is applied to monitor river ice dynamics.

Received 18 October 2006. Revision accepted 15 June 2007. Published on the NRC Research Press Web site at cjce.nrc.ca on 9 February 2008.

D. Bourgault. Department of Physics and Physical Oceanography, Memorial University, St. John's, NL A1B 3X7, Canada. (email: danielb@physics.mun.ca).

Written discussion of this article is welcomed and will be received by the Editor until 31 May 2008.

Methods

General

An experiment was designed to observe the ice variability in the St. Lawrence River, near Québec City. In this section of the river, the ice is characterized by brash ice and small floes that are modulated by the semi-diurnal tidal stream of an average amplitude of 2 $m \cdot s^{-1}$ (Canadian Hydrographic Service 1997). Over a daylight period, significant change in the ice distribution was expected, thus providing a good test for the method.

Materials and settings

The digital camera used was a commercial Canon PowerShot S70 with a maximum image size capability of 2304 × 3072 pixels (i.e., 7.1 Megapixels). It features an intervalometer that allows the user to set the camera to automatically

 doi:10.1139/L07-087

take photographs at a predefined constant interval. The time interval, τ, between successive images can be set anywhere between 1 and 60 integral minutes. A limit of 100 photos can be taken in a sequence. Therefore, the intervalometer must be reset if the experiment requires a longer time series. This camera is also equipped with a wide-angle optical-zoom lens (28–100 mm), which is a useful feature for large-scale geophysical applications. Note that many other commercial cameras are suitable for this type of work. The choice of one camera over another depends on the constraints of a particular field application (e.g., power or memory requirements, resolution required, etc.).

The camera was mounted on a tripod in room 1401 (14th floor) of the Hotel Château Frontenac, looking through the north-east window. The position was 71°12.301 W and 46°48.766 N (±17 m) and the altitude was 163 m according to a Garmin eTrex® global positioning system (GPS) unit. The error on the altitude is not provided with this GPS unit, but it could be roughly taken as 2.5 times the error on the horizontal position, i.e., about ±43 m (Garmin Product Support, personal communication, 2006).

Wide-angle images were collected at the sampling interval τ = 2 min from 0702 eastern standard time (EST) to 1628 EST on 19 January 2006, i.e., approximately from dawn to dusk. Images were stored in the Joint Photographic Experts Group (JPEG) format at the maximum possible size (i.e., 2304 × 3072 pixels) and using the lowest data compression to get the crispest images. In total, 283 images were collected, which occupied approximately 850 MB of hard memory space (each image is approximately 3 MB in size). The use of a 1 GB CompactFlash™ memory card was enough to store all images from the experiment. The battery needed to be replaced once during the experiment.

Image georectification

To extract quantitative information, the images need to be georectified. This was done by first applying the technique described by Pawlowicz (2003) for geometrically rectifying highly oblique images of ocean surface patterns. This technique requires a knowledge of the horizontal position (latitude and longitude) and altitude, H, of the camera; the view angle from north, θ; the dip angle below horizontal, λ; the tilt angle clockwise around the principal axis, ϕ; and the field of view (FOV) of the camera.

In principle, if all these parameters are known, if the camera is perfect (i.e., no lens distortion) and if the environmental conditions are ideal (i.e., no distortion caused by atmospheric processes), the images could be geometrically rectified by directly applying the Pawlowicz (2003) algorithm, without the need of ground control points (GCPs).

In practice, however, many of these parameters cannot be easily and accurately determined. Under these circumstances, GCPs and their associated image control points (ICPs) are needed. These two sets of points provide constraints on an iterative algorithm designed to find the values of the unknown parameters that minimize the root mean square (rms) distance, ϵ_{rms}, between the GCPs and the geographical positions of the ICPs after rectification. This minimization was performed with the Nelder and Mead (1965) simplex algorithm as implemented in MATLAB® (The Mathworks Inc., Novi, Mich.) data analysis and visualization software. Note that a realistic initial guess of the unknown parameters must be supplied to the algorithm, otherwise unphysical parameter values may result from the minimization. For example, the altitude, H, as provided by the GPS, even if not accurate, is a good initial guess. However, setting $H = 0$ as an initial guess may lead the algorithm to find a local minimum of ϵ_{rms} associated with a negative elevation $H < 0$, which would be unrealistic.

After applying the Pawlowicz (2003) rectification algorithm with the minimization procedure described above, there could remain a fairly large rms error between the GCPs and the rectified ICPs. This remaining error could be due to factors that are more difficult to handle geometrically (such as image distortions caused by atmospheric refraction, lens imperfection, etc.). To correct for these errors, the image is further adjusted with a regression model. The technique involves finding the polynomial surface (first or greater order) that gives a best fit to the spatial distribution of the difference between the GCPs and the geometrically rectified ICPs. This bivariate polynomial function is then removed from the position of all pixels of the image. The procedure is applied twice: once for correcting the longitudinal error and once for the latitudinal error.

As the camera was deployed on a tripod in a room protected from winds, it is assumed that it did not move during the experiment, such that each image represents exactly the same view. For this reason, the georectification procedure described above was performed on only one image and then the coordinate transformation was applied to all images. If the assumption cannot be justified, the rectification would need to be done to each image collected (in this case 283 images).

Observations

Georectification and uncertainties

A sample image is shown in Fig. 1. A portion of the channel is covered by brash ice and small floes, while other regions are free of ice. Visual inspection of this image reveals the difficulty in evaluating the ice extent. To be quantitative, the image needs to be georectified.

To perform the georectification, 11 GCPs and corresponding ICPs were identified (white crosses on Fig. 1). These were taken as features that could be unambiguously identified in the image with known geographical positions, such as wharf corners, bridge pillars, or powerline poles. The position of each of these GCPs is known to GPS accuracy (typically ±15 m).

For the georectification, the horizontal position of the camera and its FOV (= 62.5°) were fixed, but the altitude, H; the view, θ; the dip, λ; and the tilt, ϕ, angles were determined by the minimization algorithm. The algorithm resulted with the following values for these parameters: H = 99.0 m, θ = 60.3°, λ = 32.8°, and ϕ = 1.4°. Note that the number of parameters in the minimization problem could be reduced if some of the unknown parameters listed above could be measured accurately. For example, a barotropic altimeter and a total station, not used in the present study, could provide accurate H and λ measurements.

Figure 2 shows the result of this georectification applied to the image of Fig. 1. The circles represent the GCPs and

Fig. 1. An example of images collected from the Hotel Château Frontenac, room 1401, looking north-east. This image was collected at 1142 EST on 19 January 2006. The crosses identify the image control points (ICPs) associated with the ground control points (GCPs) used for image georectification.

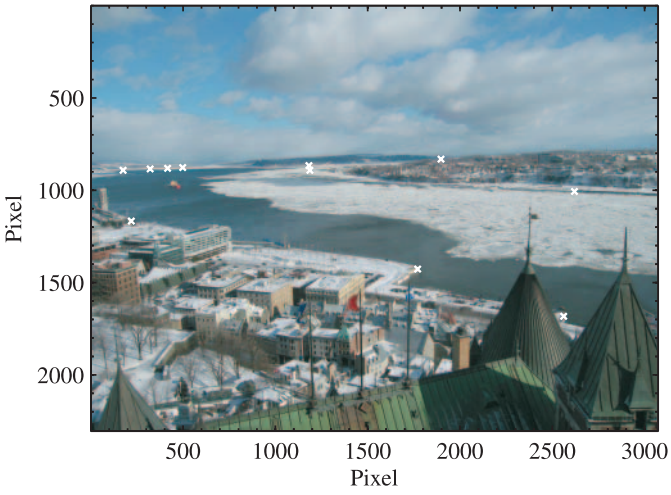

Fig. 2. The image of Fig. 1 once geometrically-rectified using the Pawlowicz (2003) method. The crosses identify the image control points (ICPs), as in Fig. 1, and the circles are the ground control points (GCPs). The dark cross in the bottom left corner indicates the location of the camera.

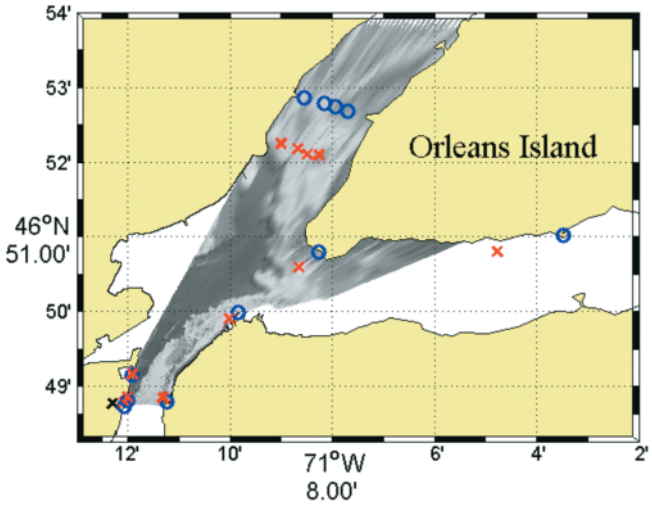

the crosses the ICPs after rectification. A perfect rectification would lead to a perfect match between the crosses and the circles. The rms distance error between the GCPs and the rectified ICPs is $\epsilon_{rms} = 744$ m. It is clear from the figure that this error is not randomly distributed amongst the GCPs, but that there is a systematic bias towards the far field GCPs. The reason for this bias is unclear. One possibility is that the algorithm reached a local rather than a global minimum. However, tests using different initial guesses for the unknown parameters always converged towards the same minimum.

Figure 3 shows the same image after applying the regression model correction based on a second-order polynomial bivariate fit of the rms error. A second-order polynomial was chosen because it resulted in a significant improvement

Fig. 3. This figure is the same as Fig. 2, but represents the condition after the regression model correction is applied. Note the alignment of the image control points (ICPs) and the ground control points (GCPs), in contrast to Fig. 2.

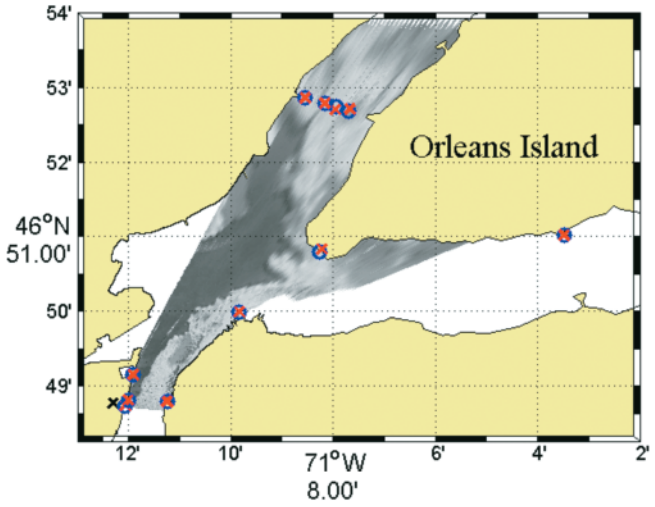

over a first-order polynomial, wheras the third-order fit produced an unphysical result with part of the image being wrapped on itself. After this adjustment, the rms distance error is reduced to $\epsilon_{rms} = 21$ m. The largest contribution to this error comes from the far field control points. The points in the near and middle field have errors less than 10 m. This error is judged acceptable for further analysis.

During rectification, the originally square image pixels become rectangular of length Δl and width Δw. The rectified pixel aspect ratios range from about $\Delta l/\Delta w \simeq 2$ for the pixels closest to the camera to $\Delta l/\Delta w \simeq 60$ in the far field ($\sim$10 km). An effective pixel resolution is then defined as

$$[1] \qquad \Delta = \sqrt{(\Delta l)^2 + (\Delta w)^2}$$

Figure 4 shows the effective pixel resolution, Δ, of the rectified image of Fig. 3. The resolution ranges from 1 m for the pixels closest to the camera to about 500 m for pixels 10 km away from the camera.

In addition to providing the effective ice floe size that can be detected as a function of distance away from the camera, the resolution map (Fig. 4) can also be interpreted as the distribution of the error uncertainty on positions. For example, given that a pixel has an effective resolution of Δ = 100 m, a small structure, such has a bridge pillar, cannot be positioned to a better accuracy than ±50 m, even though the rms distance error above ϵ_{rms} suggests a smaller uncertainty. Therefore, the Δ map also expresses the positioning error map ϵ_p, except for the region near the camera where $\Delta < 30$ m (i.e., less than twice the typical GPS accuracy of the GCPs), in which case the error stems from the GPS error and is, thus, fixed at $\epsilon_p = \pm 15$m. In summary, the ϵ_p of the georectified images is taken as

$$[2] \qquad \epsilon_p = \begin{cases} \pm\frac{1}{2}\Delta & \text{if } \Delta > 30 \text{ m}, \\ \pm 15 \text{ m} & \text{otherwise} \end{cases}$$

Fig. 4. Effective pixel resolution, Δ (in m), of the georectified images. The black cross indicates the position of the camera.

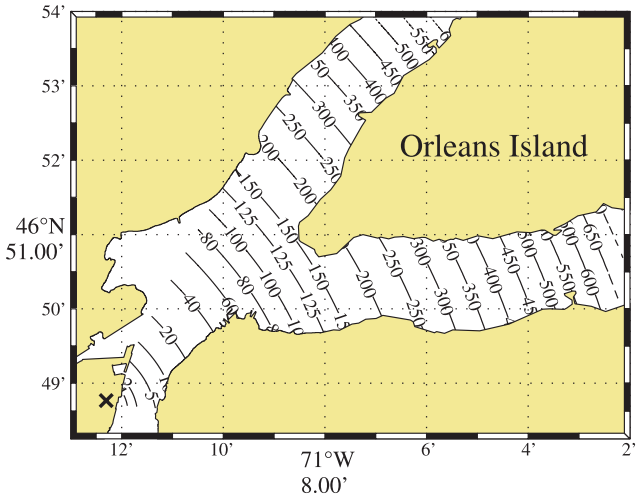

Spatiotemporal variability and uncertainties

The ice spatiotemporal variability over the effective observable region and over almost one complete semi-diurnal tidal cycle (i.e., ∼10 h) is best appreciated with animated sequences of the images, as provided as supplementary materials in Appendix A. Three animations representing three different scales, large (i.e., ∼10 km ×11 km, same as Fig. 3), meso (∼4 km × 5 km), and small (∼2 km × 2 km), are provided. The time and the image number are provided on each animation for further reference.

These animations reveal many interesting features about river ice dynamics, such as recirculating regions, horizontal shear, eddies, ice organizing into banded patterns, ice floe being rotated, ice floe aggregation, deflection of ice by Orleans Island, ice accumulation on the northern edge of Orleans Island, and more.

A close inspection of the animations reveals another source of error, mentioned at the end of the section titled Methods: the individual images do not precisely represent the same point of view. This is revealed by a small, but noticeable, spatial shift between some consecutive images of the animation. This effect is most noticeable in the far field of the large-scale animation and is barely perceptible in the meso- and small-scale animations. For example, a close examination of images 1617 and 1618 (see the large-scale animation in Appendix A), i.e., a case where this error seems largest, revealed that the images are shifted relative to each other by approximately 1 pixel. This error is presumably caused by slight camera movements of unknown origin, possibly caused by building vibrations or by distortion caused by varying atmospheric conditions. This additional error should thus be taken into account if images are to be quantitatively compared to each other.

Ice current field

The flow of ice is qualitatively clear from the animations. To be quantitative about the ice movement, a comparative analysis between two images, not necessarily immediately consecutive, is required. To achieve this, one would use a computer algorithm capable of automatically extracting the current field by comparing the changes in ice patterns between two images. One method worth exploring in this case would be the particle imagery velocity (PIV) technique, a method largely used in fluid laboratory experiments (Adrian 2005). The PIV method gives displacement vectors by finding where a pattern (i.e., a sub-area of the image) in the first image is best correlated to the second image. Pawlowicz (2003) applied the PIV method quite successfully to georectified images of sea surface patterns. The current field extracted from his images compared favorably well to ship-based current measurements.

Fig. 5. The ice current field during flood (top, 0755 EST) and ebb (bottom, 1241 EST). The vectors represent the current direction and relative intensity and the grayscale (colour in web version) represents the current magnitude ($m \cdot s^{-1}$). The error on velocity magnitude is given by (3). These fields were interpolated on a regular grid of 150 m cell size from the irregularly distributed and manually made measurements determined at the locations of the white circles. The black cross represents the camera location.

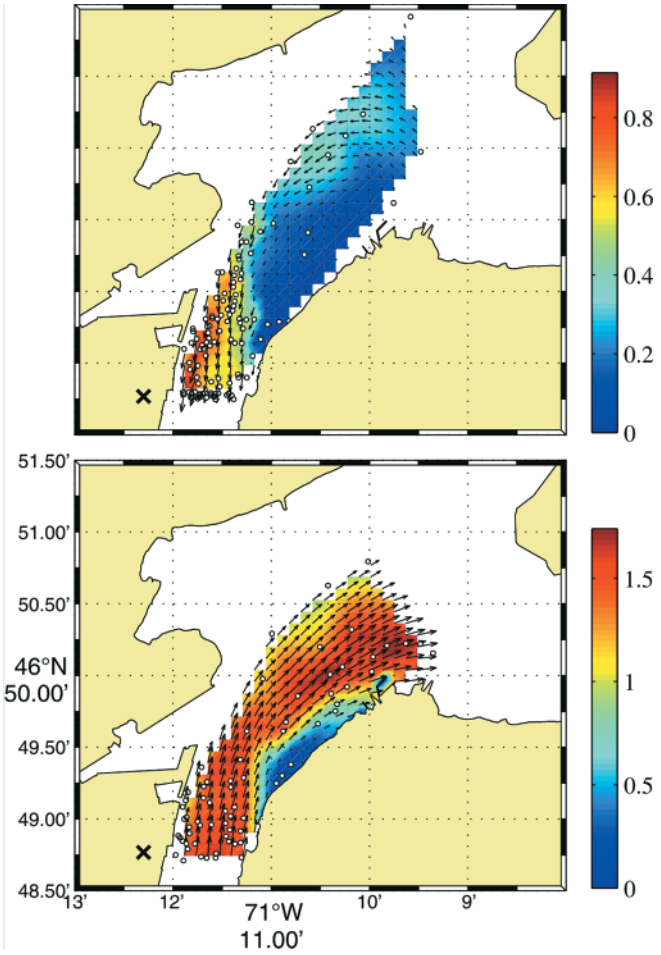

Given that the ice observed in the St. Lawrence River is quite textured, the PIV method could potentially be used to automatically extract the ice current field. Unfortunately, the PIV method applied to the images collected during this experiment proved to be inadequate due to complex moving patterns caused by cloud shadows and changing light and atmospheric conditions. The PIV could potentially work with images collected during a calm and clear day or in concert with a more sophisticated algorithm capable of discriminat-

Fig. 6. Excerpt of the ice chart produced by the Canadian Ice Service for the Québec City region (courtesy of Ice Operations, Environment Canada). This chart was produced from helicopter-based visual observations collected between 0715 EST and 1300 EST on 19 January 2006. The black dashed lines represent approximately the field of view of the camera used in this study. The thick grey (red in web version) line delimits the ice edge for easier comparison with the shore-based observations of Fig. 7.

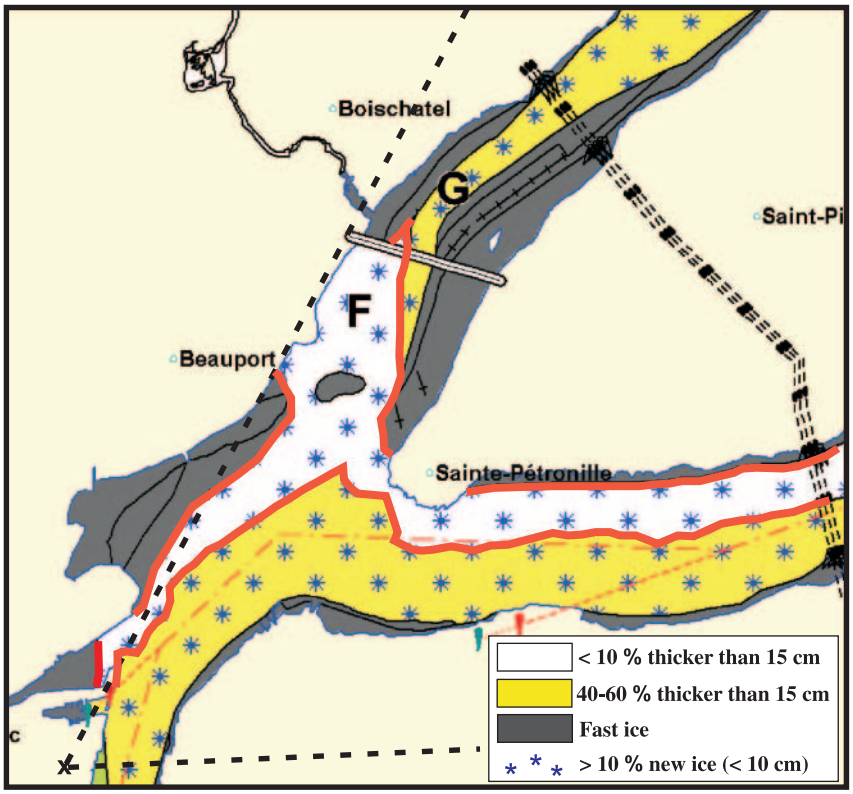

ing changes induced by ice movements from all other sources.

An alternative to using the PIV, or other sophisticated methods, is to determine manually the distance travelled by ice features (e.g., ice floes, ice edges, ice-free pools) between two images. The advantage of the method is that it is simple, robust, and accurate given our ability to recognize ice floe movements from other movements caused by cloud shadows or changing atmospheric conditions. The disadvantage is that the method cannot be automated. In any case, this manual method should be used to check any other automated methods.

Using this method, two ice current fields were determined for a time during flood and ebb. The images chosen for the analysis are image number 1570 and 1571 for flood, and 1714 and 1715 for ebb (see the animations in Appendix A). These images were chosen because there is no apparent shift between them, thus reducing the source of error discussed at the end of the previous section when images are compared. In total, 115 features during flood and 70 during ebb were identified and tracked between the images (see white circles on Fig. 5). This provided current fields that are nonuniformally distributed. From these scattered measurements, regular current fields were determined by a Delaunay triangular-based cubic interpolation, as implemented in the MATLAB® data analysis software, on a grid of 150 m square cell size. Figure 5 shows the results of this analysis.

The error in the current magnitude, ϵ_u, can be taken as the effective pixel resolution, Δ, divided by the time, T, between the frame, i.e.,

$$[3] \qquad \epsilon_u = \pm\Delta/T$$

Here, with T = 120 s, this error ranges from about ϵ_u = ±0.001 m·s^{-1} for the pixel closest to the camera to about ϵ_u = ±0.6 m·s^{-1}. Using a longer period T would result in a smaller error at the expense of time resolution.

Discussion

Figure 6 shows an excerpt of the ice chart produced by the Canadian Ice Service (CIS) for the Québec City region for 19 January 2006, the same day the shore-based images were collected. This chart was constructed from visual observations made by an ice specialist during a helicopter survey, which took place between 0715 and 1300 EST (G. Stogaitis, CIS, personal communication, 2006). The method for producing such charts is detailed in a manual produced by Environment Canada (2005).

The total area covered during this 6 h flight survey is approximately four times the area shown on Fig. 6. This suggests that it took roughly 1 to 1.5 h to collect the observations needed to produce the ice chart in Fig. 6. Therefore, the chart in Fig. 6 is not a true synoptic representation of the ice distribution, as the observations were collected over a

period sufficiently long enough to induce large changes in the ice coverage (e.g., see the large-scale animation in Appendix A). The exact time over which the observations of Fig. 6 were collected is not provided by the CIS, but is between 0715 and 1300 EST.

Comparing the CIS ice chart with the large-scale animation (Appendix A) suggests that the best correspondance is sometime between 1214 and 1226 EST. Figure 7 shows the shore-based observations at 1220 EST. Visually comparing this image with the ice chart in Fig. 6 shows fairly good qualitative agreement for the overall ice distribution and the position of the ice edge. The visual survey provides additional details, such as the ice thicknesses that are determined qualitatively by the ice specialist. On the other hand, the shore-based images provide much finer details on the ice spatial spatiotemporal distribution.

Conclusions

The results of this work show that shore-based digital imagery can provide truly synoptic, objective, and quantitative information on river ice spatiotemporal variability. One limitation of the method is that because the observations are obtained from highly oblique photographs, the resolution of the rectified images decreases rapidly as distance from the camera increases (see Fig. 4). This problem becomes more important as the degree of obliquity increases. This can be a limiting factor for remote river or lake applications where there are no structures, such as bridges and buildings, or a suitable natural embankment, such as a high river bank from where the camera can be deployed to provide the desired resolution. However, this limitation should become less of an issue as larger image size should become available to most cameras as technology advances. For example, a professional camera, such as the Canon EOS-1Ds Mark II, can provide a 16.7 Megapixel image size, which is more than twice the resolution used in this study.

Another advantage of the method proposed here is its low cost compared to satellite remote sensing or aerial surveys. As an indication, the material (camera, tripod, software) used in this study cost approximately CAN$1000 and provided around 10 h of almost continuous synoptic measurements (i.e., every 2 min) of the ice distribution over an area roughly 100 km^2. By comparison, helicopter time is approximately CAN$1000/h of flight and can, in practice, only provide quasi-synoptic observations a few times a day, at most. Synoptic observations could be provided by RADARSAT images but these are approximately CAN$1000 per image. The implementation of the method for monitoring sections of rivers proposed in this study could, therefore, lead to a more effective and efficient use of the costly survey resources.

Acknowledgments

The author would like to thank Roger Gagnon and the administration of Hotel Château Frontenac for providing access to one of their most prestigious room, Rodolphe Devillers and Rich Pawlowicz for their comments on the initial manuscript, and Alexandra Tessier and Benoit Castonguay for their technical support.

Fig. 7. Shore-based observations at 1220 EST (image number 1703). The ice distribution on this image is one of the closest to the observations made by the Canadian Ice Service (CIS) for 19 January 2006, as shown on the ice chart in Fig. 6. The thick dark (red in web version) curved line delimits the position of the ice edge for easier comparison with the CIS ice chart in Fig. 6.

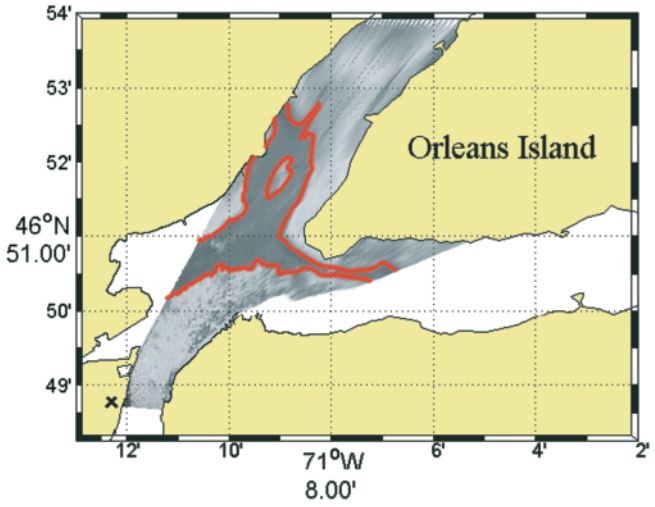

References

Adrian, R.J. 2005. Twenty years of particle image velocimetry. Experiments in Fluids, **39**(2): 159–169. doi:10.1007/s00348-005-0991-7.

Bourgault, D., and Kelley, D.E. 2003. Wave-induced boundary mixing in a partially mixed estuary. Journal of Marine Research, **61**(5): 553–576. doi:10.1357/002224003771815954.

Canadian Hydrographic Service. 1997. Atlas of tidal currents from Cap de Bon-D'esir to Trois-Rivières. Canadian Hydrographic Service, Fisheries and Oceans Canada, Government of Canada, Ottawa, Ont.

Environment Canada. 2005. MANICE: Manual of standard procedures for observing and reporting ice conditions. Environment Canada, Government of Canada, Ottawa, Ont.

Holland, K.T., Holman, R.A., Lippmann, T.C., Stanley, J., and Plant, N. 1997. Practical use of video imagery in nearshore oceanographic field studies. IEEE Journal of Oceanic Engineering, **22**(1): 81–92. doi:10.1109/48.557542.

Morse, B., Hessami, M., and Bourel, C. 2003. Characteristics of ice in the St. Lawrence River. Canadian Journal of Civil Engineering, **30**(4): 766–774. doi:10.1139/l03-030.

Nelder, J.A., and Mead, R. 1965. A simplex method for function minimization. The Computer Journal, **7**: 308–313.

Pawlowicz, R. 2003. Quantitative visualization of geophysical flows using digital oblique time-lapse imaging. IEEE Journal of Oceanic Engineering, **28**(4): 699–710. doi:10.1109/JOE.2003.819310.

Weber, F., Nixon, D., and Hurley, J. 2003. Semi-automated classification of river ice types on the Peace River using RADARSAT-1 synthetic aperture radar (SAR) imagery. Canadian Journal of Civil Engineering, **30**(1): 11–27. doi:10.1139/l02-073.

Appendix A: Supplementary materials

Figures A1 to A3 are three animations at different scales, shown below as graphics in the print version of this paper, which are available in the HTML Web version of this paper

Fig. A1. Large-scale animation (~10 km × 11 km).

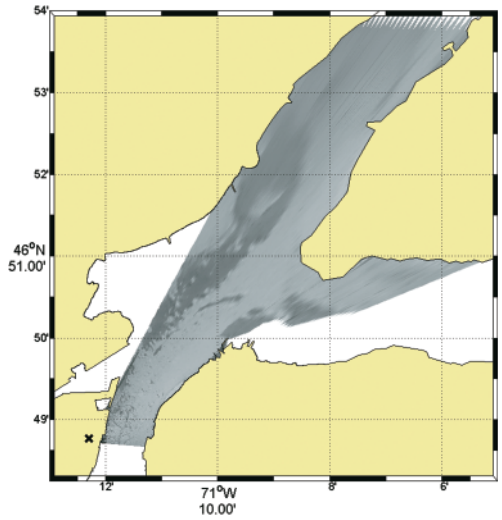

at cjce.nrc.ca (a program that plays .mov files, such as Apple QuickTime[1] or other players, is required to view these animations). Note that during the sampling period there were two periods (around 0900 and 1020 EST) where clouds and snow caused low visibility.

Fig. A2. Meso-scale animation (~4 km × 5 km).

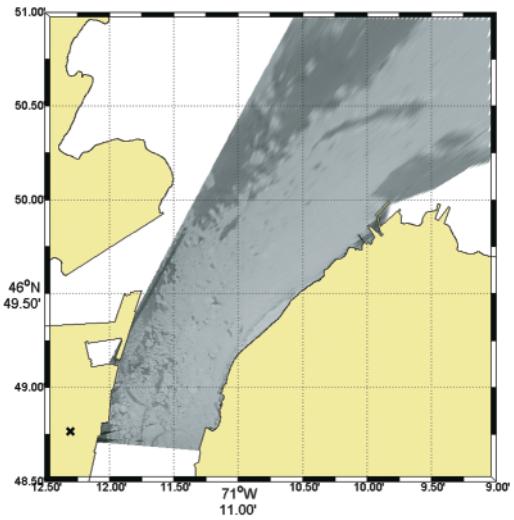

Fig. A3. Small-scale animation (~2 km × 2 km).

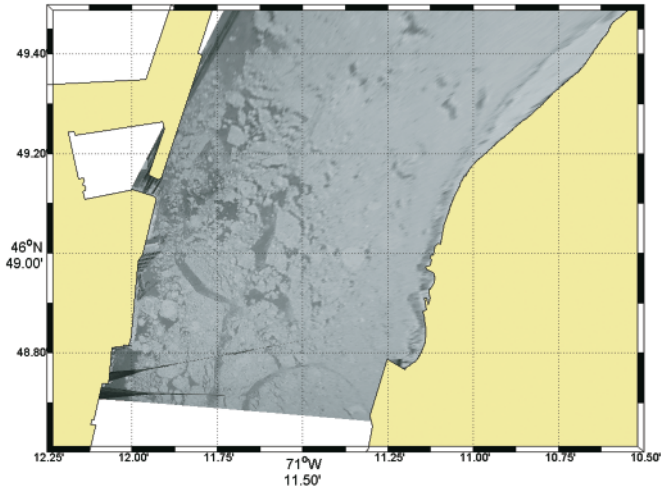

[1] Apple and QuickTime are trademarks of Apple Inc., registered in the USA and other countries. This program is available at www.apple.com/quicktime/download/.